5-12-2014

CO$_2$ Reduction under Periodic Illumination of ZnS

Ruixin Zhou
University of Kentucky, ruixin.zhou@uky.edu

Marcelo I. Guzman
University of Kentucky, marcelo.guzman@uky.edu

Right click to open a feedback form in a new tab to let us know how this document benefits you.

Follow this and additional works at: https://uknowledge.uky.edu/chemistry_facpub

Part of the Environmental Chemistry Commons, Materials Chemistry Commons, and the Physical Chemistry Commons

Repository Citation

**CO₂ Reduction under Periodic Illumination of ZnS**

Article

CO$_2$ Reduction under Periodic Illumination of ZnS

Ruixin Zhou and Marcelo I. Guzman*

Department of Chemistry, University of Kentucky, Lexington, Kentucky 40506, Unites States
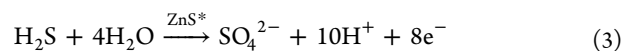
S *Supporting Information*

ABSTRACT: The photoreduction of CO$_2$ to formate (HCOO$^-$) in sphalerite (ZnS) aqueous suspensions is systematically studied in the presence of Na$_2$S hole scavenger. A series of cut-on filters at $\lambda_{cut-on} \geq 280, 295, 305, 320,$ and 400 nm are used to measure the reaction rate of formate production. The dependence of the measured reaction rates on λ_{cut-on} indicates that a wavelength of $\lambda = 345$ nm is associated with the actual bandgap of the semiconductor nanocrystallites suspended in water. The results from apparent quantum yield measurements during periodic illumination experiments suggest that (1) valence-band holes on the surface of ZnS disappear within deciseconds due to the oxidation of the scavenger while simultaneously pumping electrons to the conduction band, (2) excited electrons in the conduction band of ZnS are transferred to CO$_2$ to produce the intermediate CO$_2^{\bullet-}$, and (3) CO$_2^{\bullet-}$ abstracts a proton from water and undergoes further photoreduction on the surface of ZnS in an overall time scale for steps 2 + 3 of a few milliseconds. The separation of both process merges at ~29 ms because it decreases exponentially with a drop in [Na$_2$S] accompanied by a less negative surface potential. The behavior of the reaction rate at variable pH resembles the fraction of dissolved CO$_2$, discarding the direct participation of bicarbonate and carbonate in the reaction. Combined chromatographic, mass spectrometry, and spectroscopic studies provide new insights to understand the role of surface chemistry on the photoreduction of CO$_2$ on ZnS nanocrystals.
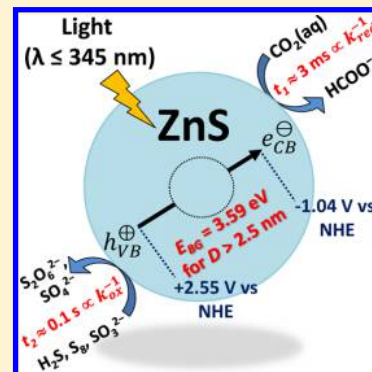
INTRODUCTION

Studying the reduction of CO$_2$ to organic compounds is an interesting problem that attracts the attention of groups that (1) aim to decrease the level of this abundant greenhouse gas in the atmosphere while simultaneously producing fuel feed-stock[1−3] or (2) pursue a mechanism of prebiotic carbon fixation through abiotic reactions.[4−6] The industrial scale conversion of CO$_2$ into fuels and the convenience of homogeneous or heterogeneous catalysis have been the subject of recent review articles.[7,8] The photocatalytic reduction of CO$_2$ in water can mainly produce formate (HCOO$^-$), formaldehyde (H$_2$CO), methanol (CH$_3$OH), and methane (CH$_4$), when semiconductor minerals such as ZnS, ZnO, CdS, or TiO$_2$ are used.[9,10] Among these minerals, the excellent reduction potential of ZnS and its low cost of production make it a viable candidate to promote CO$_2$ photoreduction in the atmospheric optical window. ZnS is a semiconductor, whose oxidizing valence-band holes are not mobile like the reducing conduction-band electrons.[11] A sacrificial reducing agent such as a sulfur-containing species, e.g., H$_2$S or SO$_3^{2-}$, both available byproducts from coal combustion, can be used to complete the electric circuit of ZnS photocatalyst for the reduction of CO$_2$ to HCOO$^-$. However, limited progress has been made in this field due to the inertness of CO$_2$ and thermodynamic impediments. A typical reaction scheme for the photoreduction of CO$_2$ in ZnS colloidal suspensions involves (1) photoexcitation of ZnS to produce excited electrons (e$^-$) and positive holes (h$^+$) (reaction 1), which can be thermally loss (reaction 2), (2) photoexcited holes can be converted by H$_2$S hole scavenger to sulfate (reaction 3), and finally (3) adsorbed CO$_2$ molecules

can accept an electron on the surface of ZnS to produce a radical anion intermediate (reaction 4) that is further reduced to HCOO$^-$ (reactions 5):

$$ZnS \xrightarrow{h\nu} e^- + h^+ \tag{1}$$

$$e^- + h^+ \rightarrow heat \tag{2}$$

$$H_2S + 4H_2O \xrightarrow{ZnS^*} SO_4^{2-} + 10H^+ + 8e^- \tag{3}$$

$$CO_2(aq) + e^- \xrightarrow{ZnS^*} CO_2^{\bullet-} \tag{4}$$

$$CO_2^{\bullet-} + H^+ + e^- \xrightarrow{ZnS^*} HCOO^- \tag{5}$$

The initial reduction of CO$_2$ proceeds through a single electron transfer to produce CO$_2^{\bullet-}$ and is accompanied by a large energy redistribution from a linear molecule to a bent radical anion.[12] The nucleophilic carbon in the surface-adsorbed radical anion abstracts a proton from water, forming a weaker acid−base pair than for the unviable oxygen radical.[12] Finally, the HCOO$^{\bullet}$ radical accepts an electron to produce HCOO$^-$.[12] The overall two-electron transfer to convert CO$_2$ to HCOO$^-$ requires a reduction potential $E° = -0.29$ V vs the normal hydrogen electrode (NHE) given in Table S1 (Supporting Information). In comparison, the conduction-band electron of ZnS is poised at -1.04 V vs NHE, and the

valence-band hole is +2.55 V vs NHE.[13] The bandgap of ZnS is 3.59 eV and varies with physical properties in the range 3.71 ± 0.13 eV (λ = 334 ± 12 nm).[13] Therefore, the theoretical energy input required from light for this surface-mediated reaction is achievable for photons with wavelength $\lambda \leq$ 345 nm.

A few previous studies of the photoreduction of CO_2 to $HCOO^-$ in aqueous suspensions of cubic ZnS nanocrystals exist.[10,14,15] However, they have not explored the photocatalytic activity of ZnS deeply. Further work is needed to understand the significance of this reduction from carbon with oxidation state +IV to +II and to provide information needed for theoretical studies of ZnS nanoparticles.[16] We report measurements of reaction rates of formate production (R_{HCOO^-}), light intensities (I_0), and apparent quantum yields of formate production at λ = 330 nm (Φ_{HCOO^-}) and simultaneously characterize the mineral during the reaction. Continuous and periodic illumination experiments yield the time scale in which reducing electrons and oxidizing holes of ZnS are transferred. The dependence of the reaction rate on the wavelength of irradiation provides a method to determine the bandgap energy of synthesized colloidal photocatalysts suspended in water. Finally, sulfide photooxidation intermediates and products are identified by high performance liquid chromatography mass spectrometry and Raman spectroscopy, and the effect of pH in the photochemical process is shown to depend on the availability of dissolved CO_2.

■ EXPERIMENTAL DETAILS

Catalyst Preparation. Colloidal ZnS suspensions were prepared based on a previous method.[17] The dropwise addition of 100 mL of 50 mM Na_2S (99.1% assay, Sigma-Aldrich) to 100 mL of 50 mM $ZnSO_4$ ($ZnSO_4 \cdot 7H_2O$, EMD, 99.5% assay) took place under stirring and purging with $N_2(g)$ (UHP, Scott-Gross). Ultrapure water (18.2 MΩ cm, Elga Purelab Flex, Veolia) purged with $N_2(g)$ was used in every step. Sulfide concentrations were determined at 1:100 dilution in a 50% volume of 2 M NaOH (99.3% assay, Fisher Chemicals) using a sulfide ion selective electrode (Thermo, Orion 94-16). The potentiometric titration with a 0.1000 M $Cd(NO_3)_2$ standard (cadmium nitrate tetrahydrate, Aldrich ≥99.0%) was used to standardize the sulfide stock employed in calibration curves. The ZnS colloidal suspension was centrifuged at 4400 rpm for 5 min (Eppendorf 5702) and rinsed twice with water to remove excess sulfate prior to irradiation.

Catalyst Characterization. Hydrodynamic particle size distributions and zeta potential (ζ) measurements were determined at variable pH using a DLS apparatus and ZetaPlus zeta potential analyzer (90 Plus/BI-MAS, Brookhaven Instruments). For pH adjustment, 1 mL of fresh ZnS supernatant was diluted in 70 mL of 1 mM Na_2S solution to bring the pH to 12, and then 0.02 M HCl (EMD Chemicals, GR ACS) was used to adjust the pH of ZnS suspensions. Undiluted samples were used for different measurements of ζ under variable [Na_2S] at pH = 7.0. The surface potential of ZnS is taken as equivalent to ζ for unchanged permittivity and viscosity in the electrical double layer.[18,19]

The absorption spectrum of scattering ZnS in water was obtained with a UV−vis spectrophotometer (Evolution 220, ISA-220 accessory, Thermo Scientific) using a built-in 10 mm silicon photodiode with a 60 mm Spectralon sphere. A 10 mm thick fused silica cuvette with water was used in the reference compartment in combination with a 1-mesh filter to subtract the background. The ISA-220 accessory was used in an alternative configuration to register the diffuse reflectance spectrum of dry ZnS powder as a Kubelka−Munk function against the certified Spectralon standard.

Photochemical Experiments. The colloidal suspensions for the photochemistry experiments were prepared just prior to use as indicated above. The addition of 0.5 mL of saturated Na_2S stock solution provided the valence-band hole scavenger and prevented any adventitious O_2 to enter the reactor. The adjusted Na_2S concentration in the suspension was ca. 8 mM, and the loading of ZnS particles was 2.3 g L^{-1}. The suspension pH was adjusted to 7 by bubbling CO_2 (UHP, Scott-Gross) before sealing the vessel containing 200 mL of the suspension. The customized fused silica photochemical apparatus consisted of a 210 mL reaction vessel outfitted with a water jacket held at 288 K (Thermo Scientific bath circulator A25). For irradiation, a collimated 1 kW high-pressure Hg (Xe) arc lamp was used after removing infrared radiation with a water filter (Scheme S1, Supporting Information). Different optical filters (all from Newport) were used when indicated. The high loading of ZnS ensures the maximum saturation of light absorption.[20] The 2.3 g L^{-1} of ZnS used in the photoreactor served as an efficient loading for the suspended particles to absorb more than 99% of the incident photon rate. The scattered photon rate measured with the detector at angles of 180° (forward scattered light), ±45°, ±90°, and ±135° is below 0.8% relative to the incident photon rate.

Measurements of the photon flux at 330 nm, performed by ferrioxalate actinometry,[21,22] were used to normalize the output of a calibrated air-cooled thermopile detector (Newport Corporation Model 818P-010-12) connected to an optical power meter (Newport Corporation Model 1918-C). This procedure has been previously demonstrated[22,23] and made possible the use of the detector to measure the light intensity of individual experiments. Factory calibration of the thermopile performed at 1064 nm using NIST standards assures a linear response of the detector within a 4.0% error for the interval 190 ≤ λ ≤ 2100 nm, which is automatically adjusted by a correction factor preloaded in the meter program. The values of Φ_{HCOO^-} at λ = 330 nm were calculated from measurements of R_{HCOO^-} and I_0 using a series of filters: (1) a neutral density filter transmitting only 34% of the light, (2) a broad band optical filter absorbing in the infrared, (3) a cut-on filter at 320 nm, and (4) a band-path filter transmitting only λ = 330 ± 10 nm. Because the measurements do not account for photon scattering, Φ values are lower limits of the quantum yields.[24] The generation of light pulses was possible by means of a combined mechanical shutter and optical chopper (Newport 75159) set by a controller (Newport model 75160) with three different blades (models 75162, 75163, and 75164). The shutter mode was used for pulsing between 0.02 and 0.5 Hz (1−25 s on period) and the chopper mode for the 10 and 2400 Hz regime (0.208−50 ms on period). A second chopper and controller (SRS model SR540) was used for pulsing in the intermediate range, between 1 and 10 Hz (0.05−0.5 s on period).

Analysis of Products. After irradiation for a selected time period, 5 mL of suspension was withdrawn from the reaction vessel through a septum, centrifuged (5 min at 4400 rpm), and the supernatant was filtered (IC Acrodisc 0.2 μm pore size; Pall Corp.). Analyses of products in the filtrate and in samples processed by solid-phase extraction (Hypersep C18, 1 mL, 100 mg) were performed by ion chromatography (IC). The second water eluent fraction of SPE cartridges preconditioned with

water and methanol were injected with an autosampler (Dionex AS) into the IC system (Dionex ICS-2000). The IC was equipped with an IonPac AS11-HC analytical column (2 × 250 mm), an IonPac AG11-HC guard column (2 × 50 mm), an ASRS-300 (2 mm) suppression module, an eluent generator (EGC III) with KOH cartridge, an anion trap column (CR-ATC), and a conductivity detector used to match the retention times of standards. The gradient separation applied a flow of 0.38 mL min^{-1} with an initial mobile phase of 1 mM KOH for 8 min followed by three linear increases of (1) 1.4 mM min^{-1} up to 15 mM, (2) 1.5 mM min^{-1} up to 30 mM, and (3) 3 mM min^{-1} up to 60 mM. After IC separation, a mass spectrometer detector (Thermo MSQ Plus) interfaced with an electrospray ionization (ESI) probe (450 °C and 70 psi N$_2$ nebulizing gas, 1.9 kV needle voltage, and 50 V cone voltage, operated in the negative mode) identified the mass-to-charge ratio (m/z) of species. An auxiliary pump (Lab Alliance) provided a flow of 0.12 mL min^{-1} methanol (Fisher Optima) mixed through a T connector with the eluent flow before aerosolization in the ESI chamber. Chromeleon and Excalibur software were used to control and process data from both systems. Concentrations were obtained from calibration curves and/or using the method of standard addition. Standards included solutions of sodium formate (Acros Organics, 99%), sodium sulfite (Fisher Chemicals, 99.9% assay) in 1% methanol, sodium sulfate (Fisher Chemicals, 99.9% assay), and sodium thiosulfate (EM Science, 97% assay).

Sulfide concentrations were potentiometrically quantified with the calibrated sulfide ion selective electrode described above. The decay of sulfide was monitored during periodic illumination experiments at λ = 330 nm to extract the decay rate constant (k_{-H_2S}). Samples withdrawn from the reactor were immediately centrifuged at 4400 rpm for 5 min, and the supernatant was treated with an equal volume of 2.0 M NaOH. The time series of sulfide decay followed first-order kinetics with correlation coefficients $r^2 \geq 0.990$.

■ RESULTS AND DISCUSSION

ZnS Characterization. The characterization of the aqueous suspensions of ZnS by dynamic light scattering (DLS), measurements of zeta potential (ζ), and the UV−vis absorption spectrum included below provides direct information to understand the surface photoreactions of interest. The findings in this paper indicate that surface species dominate the reduction of CO$_2$ and the oxidation of the hole scavenger.

Noninvasive DLS reports particle sizes such as those present during the experiments in aqueous conditions (Figure 1), avoiding filtering and drying preparation steps needed in XRD and TEM, which could result in the oxidation and change in the surface charge of ZnS. The effect of acidification on particle size and surface charge in ZnS colloidal suspensions—sequential addition of acid reduced the pH of these suspensions from 12.0 to 2.3—is also shown in Figure 1. The measurements applied DLS to compare the diffusion of particles in the colloidal suspension. In addition, the crystallite size D from the XRD pattern (Figure S1, Supporting Information) and transmission electron microscopy (TEM) images are not exactly the same of the particle size obtained by DLS (Figure 1) because ZnS particles in suspension are made up of several different crystallites.

The intensity correlation function of each sample was measured over three runs at a scattering angle of 90° from the
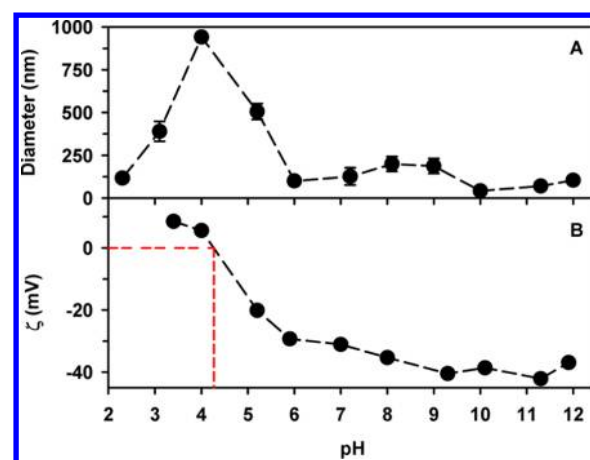
Figure 1. (A) Particle size distribution (diameter) and (B) zeta potential (ζ) of synthesized ZnS colloidal suspensions at 20 °C and variable pH.

incident laser (λ = 658 nm) beam. Particles with size between 35 and 950 nm were detected at pH 10 and 4, respectively (Figure 1A). The particle size is described by a unimodal distribution for the whole pH range. The synthesized ZnS at 20 °C initially experiences slight changes of aggregate size, but the distribution remains unimodal with diameters of 40−200 nm down to pH 5.9. It should be noted that further acidification led to considerable larger particles for the pH range 3.1−5.1 and peaks at pH = 4.0 to a value of 940 nm. No considerable difference in the particle size distribution was observed for ZnS synthesized at 5, 20, or 40 °C.

The negative values for the zeta potential in Figure 1B with magnitude larger than the boundary of −30 mV, in the range of pH 7.0−12.0, indicate that the particles of ZnS repeal each other, and there is no tendency to flocculate. As the pH drops below 5.9, the suspension becomes less stable and the zeta potential becomes increasingly less than −30 mV; thus, there is no force to prevent the particles coming together and flocculation occurs. The continuous addition of dilute HCl eventually neutralizes the negative charge at the isoelectric point of pH = 4.2 ± 0.1 obtained by interpolation (red dashed line in Figure 1B). Further addition of acid results in a buildup of positive charge. For the syntheses at 5 and 40 °C, the isoelectric point is within the ±0.1 range of pH measured at 20 °C.

The characterization of dry ZnS by other techniques could be affected by processes occurring in bulk and aggregated catalyst. This information for X-ray diffraction (XRD) patterns (Figure S1) and Raman spectroscopy (Figure S2) during the reaction, transmission electron microscopy (TEM) and energy-dispersive X-ray spectroscopy (EDS) (Figure S3), and Brunauer−Emmett−Teller (BET) measurements can be found in the Supporting Information.

Identification of Products. Figure 2 shows the species identified as anions in the chromatogram for irradiation at λ > 200 nm. Peaks elute in the following order: formate (HCOO$^-$, m/z = 45), bicarbonate (HCO$_3^-$, m/z = 61), bisulfite (HSO$_3^-$, m/z = 81), bisulfate (HSO$_4^-$, m/z = 97), hydrogen thiosulfate (HS$_2$O$_3^-$, m/z = 113), and hydrogen dithionate (HS$_2$O$_6^-$, m/z = 161). The same products were observed for irradiation with the different cut-on filters ($\lambda_{cut-on} \geq$ 280, 295, 305, and 320 nm) and for monochromatic light (λ = 330 nm). Control experiments that demonstrate the heterogeneous photo-
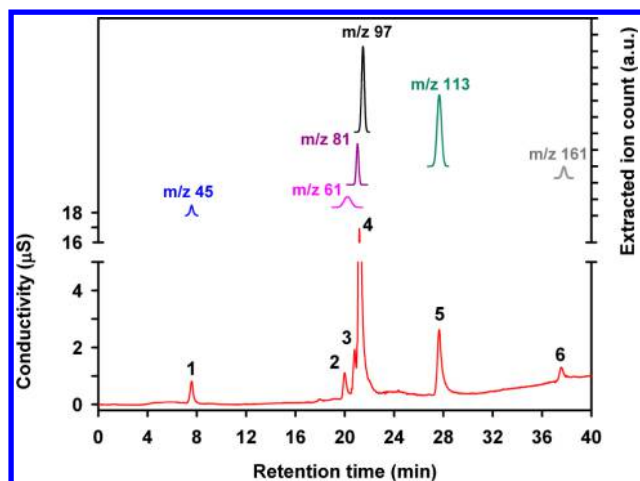
Figure 2. Ion chromatogram of a sample photolyzed ($\lambda > 200$ nm) for 1.5 h showing peaks of (1) formate ($HCOO^-$, $m/z = 45$), (2) bicarbonate (HCO_3^-, $m/z = 61$), (3) bisulfite (HSO_3^-, $m/z = 81$), (4) bisulfate (HSO_4^-, $m/z = 97$), (5) hydrogen thiosulfate ($HS_2O_3^-$, $m/z = 113$), and (6) hydrogen dithionate ($HS_2O_6^-$, $m/z = 161$).

production of formate on the surface of the ZnS semiconductor were carried out in the presence of one or more of colloid (ZnS), ultraviolet light ($h\nu$; $\lambda > 200$ nm), carbon dioxide (CO_2), and sulfur-based hole scavenger (S_T). In the absence of ZnS, there is no production of formate (control A). The negative result for the production of formate under dark conditions (control B) indicates that a thermal mechanism is not the cause of this reaction. No formate production was observed unless CO_2 as an electron acceptor (control C) and sulfide hole scavenger as an electron donor (control D) were present.

The oxidation of sulfide hole scavenger during the reaction also produces a small amount of yellow colloid visually observed during irradiation and identified as elemental (rhombic) sulfur, S_8, in the Raman spectrum (Figure S2, Supporting Information).[25] This species is not derived from the catalyst that remains intact as shown by XRD and TEM data (Supporting Information). Rhombic sulfur is as an oxidation intermediate produced by the sulfide hole scavenger. The simultaneous photooxidation and substitution mechanism below protects the integrity of ZnS, consumes solution-phase sulfide ions in the system, and produces elemental sulfur:[26]

$$ZnS + 2h^+ \rightarrow Zn^{2+} + S \tag{5}$$

$$Zn^{2+}S + HS^- \rightarrow ZnS + S + H^+ \tag{6}$$

$$2h^+ + HS^- \rightarrow S + H^+ \tag{7}$$
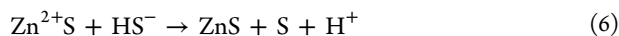
Given the dissociation of H_2S ($pK_{a1} = 7.05$ and $pK_{a2} = 14.92$ at 25 °C),[27] both available acidic species at pH = 7 (dissociation fraction $\alpha_{H_2S} = 0.53$ and $\alpha_{HS^-} = 0.47$) may participate as initial hole scavenger. However, neutral H_2S should be the main reductant because HS^- is repelled by the negatively charged surface of ZnS for higher pH than the isoelectric point of ZnS (pH = 4.2, Figure 1). CO_2 is reduced to $HCOO^-$ in the conduction band of ZnS, while all involved sulfur species participate in oxidation reactions at the valence band. S_8, $S_2O_3^{2-}$, SO_3^{2-}, and $S_2O_6^{2-}$ (Scheme 1) are formed as intermediate products during the oxidation of sulfide toward SO_4^{2-} with the possible transfer of electrons summarized in Table S2 (Supporting Information).

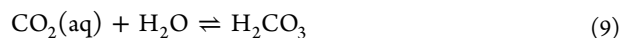**Scheme 1. Representation of the Heterogeneous Photocatalysis on ZnS Nanoparticles in Water**
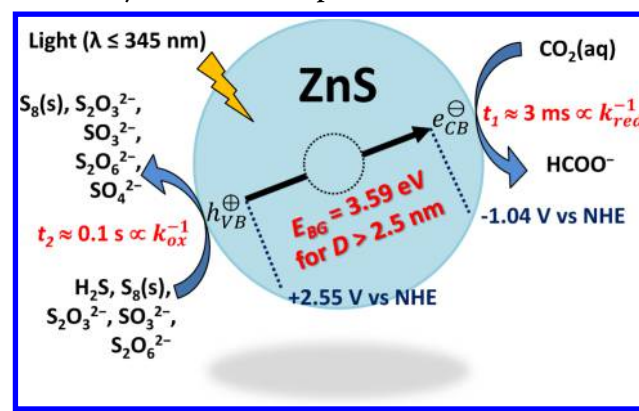
$S_2O_3^{2-}$ is assumed to be an oxidation intermediate directly formed at the valence band. S_8 may react with H_2 to regenerate H_2S, while the formation of dithionate ($S_2O_6^{2-}$) may also be the result of SO_3^{2-} oxidation.[27,28] A summary of the redox potentials for some of the reactions observed is given in Table S1 (Supporting Information). The photoexcited state ZnS* can reduce any of the species on the left-hand side of the equations in Table S1, as well as to oxidize any of the species on the right-hand side.
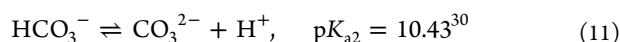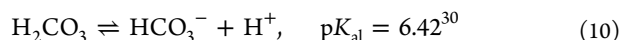
Bangap from Chemical Measurements and Identification of CO_2 as the Reactive Species. The production of $HCOO^-$ vs time, in the presence of sulfide hole scavenger, is shown in Figure 3. These experiments utilized different cut-on filters at wavelengths $\lambda_{cut-on} \geq 280$, 295, 305, 320, and 400 nm. For $\lambda_{cut-on} \geq 400$ nm, no $HCOO^-$ production occurred.
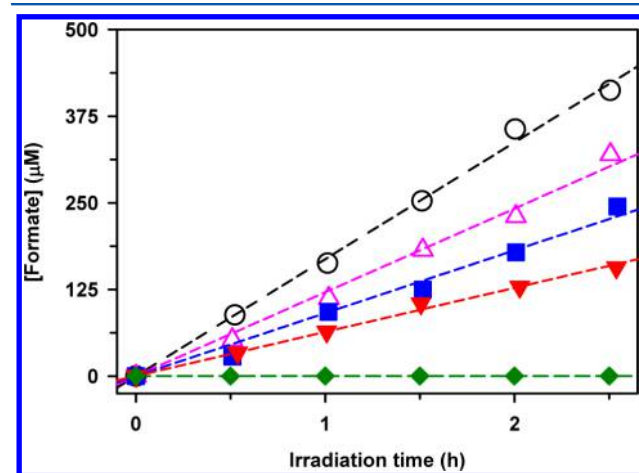
Figure 3. Formate production at variable cut-on wavelength of irradiation (λ_{cut-on}). The reaction rate at $\lambda_{cut-on} \geq 280$ (O), 295 ($\triangle$), 305 ($\blacksquare$), and 320 nm ($\blacktriangledown$) is 162.07, 120.29, 95.48, and 63.61 μM h^{-1}, respectively. No formate production observed for $\lambda_{cut-on} \geq 400$ nm ($\blacklozenge$).

Upon dissolution of gaseous CO_2 in water at 15 °C (Henry's law constant $K_H = [CO_2(aq)]/P_{CO_2} = 0.0260$ mol L^{-1} atm^{-1} at 15 °C)[29] several species coexist in equilibrium:

$$CO_2(g) \rightleftharpoons CO_2(aq) \tag{8}$$

$$CO_2(aq) + H_2O \rightleftharpoons H_2CO_3 \tag{9}$$

$$H_2CO_3 \rightleftharpoons HCO_3^- + H^+, \quad pK_{a1} = 6.42^{30} \qquad (10)$$

$$HCO_3^- \rightleftharpoons CO_3^{2-} + H^+, \quad pK_{a2} = 10.43^{30} \qquad (11)$$

and only a negligible amount of all dissolved CO_2 (CO_2(aq) + H_2CO_3) is in the form H_2CO_3. The species present in the previous equilibrium system (Figure 4) depend on pH as
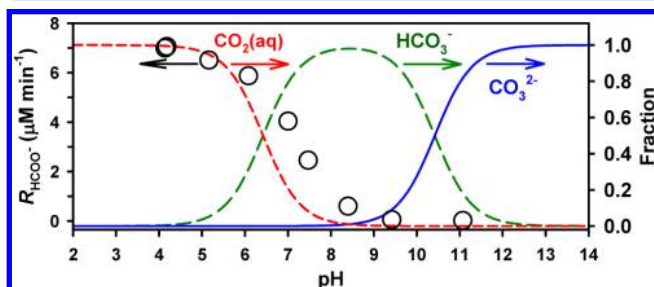
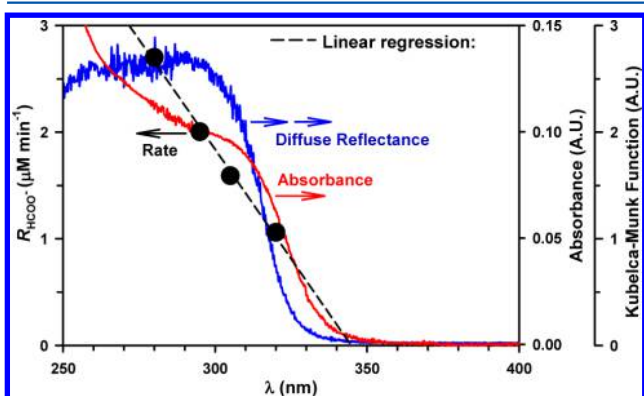**Figure 4.** Rate of formate production (R_{HCOO^-}) and fraction of dissolved CO_2, HCO_3^-, and CO_3^{2-} present in equilibrium vs pH at 15 °C.

follows: (1) At pH < pK_{a1} = 6.42 dissolved CO_2 is dominant and (2) at pH > pK_{a2} = 10.43 carbonate is dominant, while (3) for intermediate pH values (pK_{a1} < pH < pK_{a2}) bicarbonate is the main species. The dependence of R_{HCOO^-} on pH. (Figure 4) under full lamp irradiation resembles the fraction of total dissolved CO_2 present in equilibrium, indicating that CO_2 is the only species that controls the process. The charged species (HCO_3^- and CO_3^{2-}) are not primary reagents undergoing photoreduction.

This observation agrees with a model of reactive surface species adsorbed to the negatively charged surface of ZnS (Langmuir–Hinshelwood mechanism), which prefers the interaction with neutral dissolved CO_2 over the electrostatic repulsion to HCO_3^- and CO_3^{2-} anions. However, an Eley–Rideal mechanism cannot be completely discarded.[31−33]

A narrow particle size distribution is confirmed by the sharp drop observed in the reflectance spectrum of dry ZnS powder with reflection edge at λ = 300 nm (Figure 5). The associated valence band of the dry ZnS powder has a bandgap of 3.76 eV (λ = 330 nm), which is blue-shifted from the absorption edge of wet (bulk) ZnS at λ = 345 nm (Figure 5). The absorption band edge is centered at λ = 312 nm in the ZnS suspension in water


Figure 5. Rate of formate production (R_{HCOO^-}) vs cut-on wavelength of irradiation at pH = 7.0. Absorption spectrum of ZnS in water (red line and internal right axis) and diffuse reflectance spectrum of dry ZnS powder (blue line and external right axis).

(Figure 5). Although the particles could experience quantum size effects,[34] the experiments take place in water, and the absorption spectrum of ZnS colloidal suspensions is needed to estimate the bandgap energy under actual experimental conditions. The slopes in Figure 3 give the R_{HCOO^-} values plotted in Figure 5 vs specific λ_{cut-on} of irradiation. The bandgap of ZnS colloidal suspensions can be better determined from the extrapolated straight line in Figure 5.

This is the first time that such a determination of the bandgap is made based on the measurement of reaction rates and irradiation wavelengths. The equation for the linear regression in Figure 5 is R_{HCOO^-} (μM min^{-1}) = 14.152 − 0.0410 × λ_{cut-on} (nm) with a coefficient of correlation r^2 = 0.995. The reaction rate falls to zero (R_{HCOO^-} = 0) for an extrapolated cut-on wavelength λ_{cut-on} = 345 nm. The value of λ_{cut-on} = 345 nm is in excellent agreement with the absorption spectrum for the ZnS colloidal suspension (red line in Figure 5), registered from the supernatant remaining in solution after centrifugation of the 2.3 g L^{-1} ZnS colloidal suspension (DLS yields D = 51 ± 2 nm). Remarkably, the absorption spectrum in Figure 5 falls to zero above the same λ_{cut-on}. The bandgap energy for ZnS suspension in water is calculated using the equation $E_{BG} = hc\lambda_{cut-on}^{-1}$ = 5.74 × 10^{-19} J ≡ 3.59 eV, where h = 6.626 × 10^{-34} J s is the Plank constant and c = 3.0 × 10^8 m s^{-1} is the speed of light. The measured E_{BG} for nanoparticles in water is within the range of previous reports for ZnS,[13] and it does not display quantum size effects, as expected for diameters larger than the Bohr radius of ZnS (2.50 nm).[35]

For continuous monochromatic irradiation at λ = 330 nm, the ratio of R_{HCOO^-} = 5.92 × 10^{-9} mol L^{-1} s^{-1} to I_0 = 4.10 × 10^{-7} einstein L^{-1} s^{-1} (measured by actinometry), yields Φ_{HCOO^-} = 1.44% as a lower limit of the quantum yield, because light is extinguished both by absorption of the photocatalyst and by light scattering from the particles in suspension.[24] This monochromatic Φ_{HCOO^-} should not be compared to those larger values also reported by ferrioxalate actinometry (e.g., for ZnS and MnS)[15,36] employing broadband irradiation (200−400 nm). Care must also be taken when comparing our measurement to the higher Φ_{HCOO^-} = 20% at λ = 280 nm.[37] More importantly, several factors could affect Φ_{HCOO^-} in different experimental setups, making the comparison of Φ_{HCOO^-} by different groups difficult.[38] Particularly, experimental systems could have different (1) intensity of monochromatic illumination, (2) pH, (3) mass transport (e.g., stirring rate in the reactor), and (4) cell geometry.[38] In addition, the structure and associated catalyst properties could vary to considerably affect the observed Φ_{HCOO^-}.[38] For example, whether the experimental preparation skipped the final steps after the synthesis (centrifugation, washing, and rinsing of the catalyst with water), the reaction rate at λ = 330 nm increased to R_{HCOO^-} = 3.72 × 10^{-8} M s^{-1}, representing a 6.3 times more efficient process with Φ_{HCOO^-} = 9.07%. The Φ_{HCOO^-} values reported are useful to compare the set of reactions occurring under similar conditions for the specific structure characterized. Overall, the information derived from the Φ_{HCOO^-} values in the section below is of general application to the photocatalyst and enabled the determination of the lifetime of surface redox carriers.

Lifetime of Redox Carriers on the Surface of Photoexcited ZnS. Figure 6A shows the changes in Φ_{HCOO^-} (at pH = 7.0) under periodic illumination with alternate and equally lasting bright (τ_L) and dark (τ_D) intervals. In Figure 6A, for the upper limit chopper frequencies examined, $\Phi_{L\rightarrow0}$ merges with
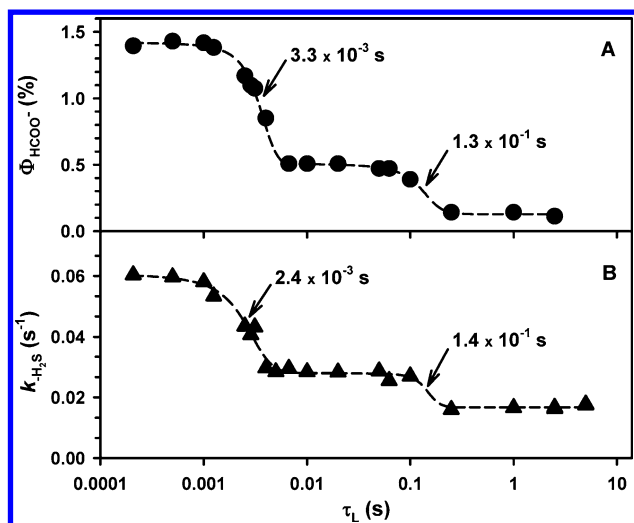
Figure 6. (A) Apparent quantum yield of formate production (Φ_{HCOO^-}) and (B) first-order rate constant of sulfide decay k_{-H_2S} vs the bright interval time under periodic illumination (τ_L) at pH = 7.0 and $[Na_2S]_0$ = 2.0 mM.

the value measured under continuous illumination (Φ_{HCOO^-} = 1.44%). However, two well-resolved inflection points are observed when transitioning from $\Phi_{L \to 0}$ to the lower limit chopper frequencies ($\Phi_{L \to \infty}$), which correspond to redox carriers with different reactivity.[39] The two inflection points fitted with a nonlinear least-squares regression for a double sigmoid curve occur at t_1 = 3.3 ms and t_2 = 0.13 s (Figure 6A) for $[Na_2S]_0$ = 2.0 mM and pH = 7.0 and can be associated with the transfer of reducing conduction-band electrons and the oxidizing valence holes acting over sulfide, respectively. Close values of t_1 = 2.4 ms and t_2 = 0.14 s (to those obtained by measuring Φ_{HCOO^-} = R_{HCOO^-}/I_0) are potentiometrically determined from the first-order rate constant for sulfide decay (k_{-H_2S}), a stable species in dark controls (Figure 6B).

Experiments at variable initial $[Na_2S]$ are useful to investigate which transition corresponds to oxidizing and reducing species. The measured surface area of ZnS assures experimental conditions of submonolayer coverage by the hole scavenger for $[Na_2S]$ < 65 mM. Both transitions t_1 and t_2 are still observed in the range 0.50 ≤ $[Na_2S]$ ≤ 16.9 mM. These experiments provided a method to relate the two transitions with the concentration of the reducing species and the measured surface potential,[18,19,39,40] by assuming that the Butler−Volmer (BV) equation[18,19,39,40] holds for illuminated ZnS colloids. The faster photon absorption rate by ZnS than the loss of reducing electrons and oxidizing holes by ZnS* creates an excess redox potential (E) and surface charge. The previous imbalance affects the half-reduction and half-oxidation rate constants of ZnS[39,40] $k_{red} = k_0 e^{-[\alpha_{red}nF/RT](E-E\circ)}$ and $k_{ox} = k_0 e^{(\alpha_{ox}nF/RT)(E-E\circ)}$, respectively, where $E°$ is the standard redox potential, R is the gas constant, F is the Faraday constant, T is the absolute temperature, n_{red} and n_{ox} are the number of electrons transferred in each half-reaction, k_0 is the standard heterogeneous rate constant, and α_{red} and α_{ox} are the dimensionless charge transfer coefficients.[39,40] In our experiments, the potential is affected by changing the concentration of the reducing species in the range 0.50 ≤ $[Na_2S]_0$ ≤ 16.9 mM, what modifies the surface potential of ZnS (Figure S5, Supporting

Information) as represented by ζ for unchanged permittivity and viscosity in the electrical double layer.[18,19]

Figure 7A shows, as expected, both transitions t_1 and t_2 have opposite trends with increasing $[Na_2S]$. Analogously, Figure 7B
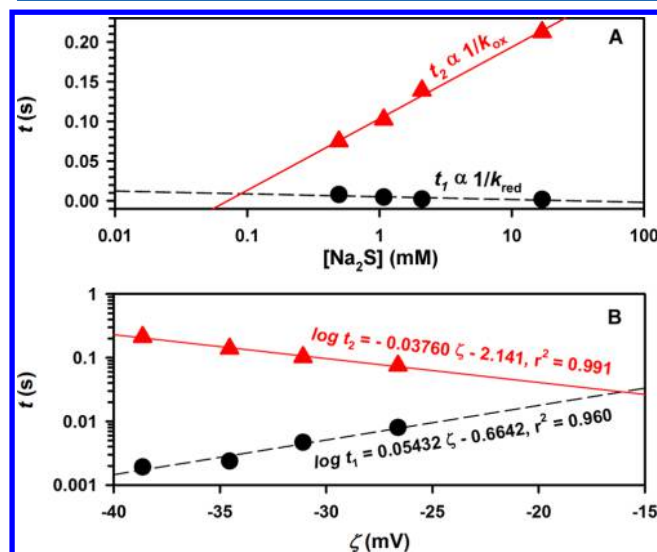
Figure 7. Transitions (●) t_1 and (▲) t_2 vs (A) variable $[Na_2S]_0$ and (B) zeta potential (ζ). The red and black-dashed lines show the linear least-squares regressions, which intercept for (A) a coverage of $[Na_2S]$ = 90 μM, corresponding to (B) an extrapolated ζ = −16 mV and t = 29 ms.

indicates the same kind of dependence for the transitions on ζ. The experimental information in Figure 7A demonstrates how the two photoredox transitions observed are related to the rate constants k_{red} and k_{ox}, which are reciprocal to t_1 and t_2, respectively: $t_1 \propto k_{red}^{-1}$ and $t_2 \propto k_{ox}^{-1}$. Given the previous inverse relationships, and the positive exponential form of k_{ox}, an increase in the concentration of hole scavenger (or the potential) predicts an increase in the value of t_2 with $[Na_2S]$ in Figures 7A and its decrease in Figure 7B with ζ. The intersection point of both regression lines in Figure 7B predicts that both transitions become undistinguishable for a surface potential of −16 mV at 29 ms. On the contrary, the measured t_1 value decreases with $[Na_2S]$ and increases for larger ζ (Figure 7B) due to the negative exponential form describing k_{red}. This interpretation of t_1 being related to k_{red} is in agreement with the recently reported higher rate of reduction for $H_2(g)$ generation in CdS nanocrystals.[41] The higher rate of $H_2(g)$ production observed followed an exponential function for more negative potentials.[41]

■ CONCLUSIONS

Remarkably, the reactive intermediates in the photoexcited semiconductor exist for relative long times,[39] as observed here for ZnS*. Characteristic surface carriers remain active for less than 10 and 215 ms for the transfer of mobile electrons and loss of fixed holes, respectively. In other words, the reactive carriers can be detected for longer time scales than the range explored (e.g., 150 fs ≤ $\tau_{1/2}$ < 100 μs)[42] during time-resolved spectroscopy studies of semiconductors. The photoreduction of CO_2 to $HCOO^-$ in aqueous colloidal suspensions of ZnS in the presence of Na_2S directly consumes dissolved CO_2 as the reactive species adsorbed to the surface of ZnS. A new method to report the bandgap of the semiconductor in the actual

hydrated state is demonstrated based on the dependence of the reaction rate on the wavelength of irradiation. The measurement of quantum yields under periodic illumination offers mechanistic information that provides the time scale (10^{-3}–10^{-1} s) of redox processes on the surface of ZnS, which occur at several orders of magnitude slower than excitation of ZnS. Further studies of this system are underway with the goals of comparing catalyst stability, improving efficiency, and replacing the sacrificial electron donor by other species.

ASSOCIATED CONTENT

Ⓢ Supporting Information

Additional experimental details, tables, and figures. This material is available free of charge via the Internet at http://pubs.acs.org.

AUTHOR INFORMATION

Corresponding Author
*E-mail marcelo.guzman@uky.edu; Tel 859-323-2892 (M.I.G.).

Notes

The authors declare no competing financial interest.

ACKNOWLEDGMENTS

ABBREVIATIONS

DLS, dynamic light scattering; $E°$, standard reduction potential; E_{BG}, bandgap; h^+, oxidizing hole; NHE, normal hydrogen electrode; R_{HCOO^-}, rate of formate production; I_0, light intensity; Φ_{HCOO^-}, apparent quantum yield of formate production; ζ, zeta potential.

REFERENCES

(1) Kumar, B.; Llorente, M.; Froehlich, J.; Dang, T.; Sathrum, A.; Kubiak, C. P. Photochemical and Photoelectrochemical Reduction of CO_2. *Annu. Rev. Phys. Chem.* **2012**, *63*, 541−569.

(2) Costentin, C.; Robert, M.; Saveant, J.-M. Catalysis of the Electrochemical Reduction of Carbon Dioxide. *Chem. Soc. Rev.* **2013**, *42*, 2423−2436.

(3) Boston, D. J.; Xu, C.; Armstrong, D. W.; MacDonnell, F. M. Photochemical Reduction of Carbon Dioxide to Methanol and Formate in a Homogeneous System with Pyridinium Catalysts. *J. Am. Chem. Soc.* **2013**, *135*, 16252−16255.

(4) Guzman, M. I.; Martin, S. T. Photo-production of Lactate from Glyoxylate: How Minerals Can Facilitate Energy Storage in a Prebiotic World. *Chem. Commun.* **2010**, *46*, 2265−2267.

(5) Guzman, M. I.; Martin, S. T. Oxaloacetate-to-Malate Conversion by Mineral Photoelectrochemistry: Implications for the Viability of the Reductive Tricarboxylic Acid Cycle in Prebiotic Chemistry. *Int. J. Astrobiol.* **2008**, *7*, 271−278.

(6) Guzman, M. I.; Martin, S. T. Prebiotic Metabolism: Production by Mineral Photoelectrochemistry of α-Ketocarboxylic Acids in the Reductive Tricarboxylic Acid Cycle. *Astrobiology* **2009**, *9*, 833−842.

(7) Artero, V.; Fontecave, M. Solar Fuels Generation and Molecular Systems: Is it Homogeneous or Heterogeneous Catalysis? *Chem. Soc. Rev.* **2013**, *42*, 2338−2356.

(8) de Richter, R. K.; Ming, T. Z.; Caillol, S. Fighting Global Warming by Photocatalytic Reduction of CO_2 Using Giant Photocatalytic Reactors. *Renew. Sust. Energy Rev.* **2013**, *19*, 82−106.

(9) Hoffmann, M. R.; Moss, J. A.; Baum, M. M. Artificial Photosynthesis: Semiconductor Photocatalytic Fixation of CO_2 to Afford Higher Organic Compounds. *Dalton Trans.* **2011**, *40*, 5151−5158.

(10) Eggins, B. R.; Robertson, P. K. J.; Murphy, E. P.; Woods, E.; Irvine, J. T. S. Factors Affecting the Photoelectrochemical Fixation of Carbon Dioxide with Semiconductor Colloids. *J. Photochem. Photobiol., A* **1998**, *118*, 31−40.

(11) Nakaoka, Y.; Nosaka, Y. Electron Spin Resonance Study of Radicals Produced by Photoirradiation on Quantized and Bulk ZnS Particles. *Langmuir* **1997**, *13*, 708−713.

(12) Wenzhen, L. Electrocatalytic Reduction of CO_2 to Small Organic Molecule Fuels on Metal Catalysts. In *Advances in CO_2 Conversion and Utilization*; American Chemical Society: Washington, DC, 2010; Vol. *1056*, pp 55−76.

(13) Xu, Y.; Schoonen, M. A. A. The Absolute Energy Positions of Conduction and Valence Bands of Selected Semiconducting Minerals. *Am. Mineral.* **2000**, *85*, 543−556.

(14) Kanemoto, M.; Shiragami, T.; Pac, C.; Yanagida, S. Semiconductor Photocatalysis. Effective Photoreduction of Carbon Dioxide Catalyzed by ZnS Quantum Crystallites with Low Density of Surface Defects. *J. Phys. Chem.* **1992**, *96*, 3521−3526.

(15) Zhang, X. V.; Ellery, S. P.; Friend, C. M.; Holland, H. D.; Michel, F. M.; Schoonen, M. A. A.; Martin, S. T. Photodriven Reduction and Oxidation Reactions on Colloidal Semiconductor Particles: Implications for Prebiotic Syntheis. *J. Photochem. Photobiol., A* **2007**, *185*, 301−311.

(16) Feigl, C.; Russo, S. P.; Barnard, A. S. Safe, Stable and Effective Nanotechnology: Phase Mapping of ZnS Nanoparticles. *J. Mater. Chem.* **2010**, *20*, 4971−4980.

(17) Yanagida, S.; Ishimaru, Y.; Miyake, Y.; Shiragami, T.; Pac, C. J.; Hashimoto, K.; Sakata, T. Semiconductor Photocatalysis 7. ZnS-Catalyzed Photoreduction of Aldehydesand Related Derivatives - 2-Electron-Transfer Reduction and Relationship with Spectroscopic Properties. *J. Phys. Chem.* **1989**, *93*, 2576−2582.

(18) Kirby, B. *Micro- and Nanoscale Fluid Mechanics: Transport in Microfluidic Devices*; Cambridge University Press: Cambridge, UK, 2010.

(19) Delgado, A. V.; Gonzalez-Caballero, F.; Hunter, R. J.; Koopal, L. K.; Lyklema, J. Measurement and Interpretation of Electrokinetic Phenomena. *J. Colloid Interface Sci.* **2007**, *309*, 194−224.

(20) Kisch, H. On the Problem of Comparing Rates or Apparent Quantum Yields in Heterogeneous Photocatalysis. *Angew. Chem., Int. Ed.* **2010**, *49*, 9588−9589.

(21) Kuhn, H. J.; Braslavsky, S. E.; Schmidt, R. Chemical Actinometry. *Pure Appl. Chem.* **2004**, *76*, 2105−2146.

(22) Hatchard, C. G.; Parker, C. A. A New Chemical Actinometer. II Potassium Ferrioxalate as a Standard Chemical Actinometer. *Proc. R. Soc.* **1956**, *A235*, 518−536.

(23) Wolf, H. P.; Bohning, J. J.; Schnieper, P. A.; Weiss, K. Apparatus for the Measurement of Quantum Yields and Rates of Photochemical Reactions. *Photochem. Photobiol.* **1967**, *6*, 321−329.

(24) Serpone, N. Relative Photonic Efficiencies and Quantum Yields in Heterogeneous Photocatalysis. *J. Photochem. Photobiol., A* **1997**, *104*, 1−12.

(25) Nilsen, W. G. Raman Spectrum of Cubic ZnS. *Phys. Rev.* **1969**, *182*, 838−850.

(26) Becker, W. G.; Bard, A. J. Photoluminescence and Photoinduced Oxygen Adsorption of Colloidal Zinc Sulfide Dispersions. *J. Phys. Chem.* **1983**, *87*, 4888−4893.

(27) House, J. E.; House, K. A. *Descriptive Inorganic Chemistry*, 2nd ed.; Elsevier: San Diego, 2010.

(28) Katagiri, A.; Arai, H.; Takehara, Z. Mechanism of the Electrooxidation of Sulfite Catalyzed by Copper Ion. *J. Electrochem. Soc.* **1995**, *142*, 2899−2905.

(29) *Standard Reference Database 69: The NIST Chemistry WebBook*; Mallard, W. G., Linstrom, P. J., Eds.; National Institute of Standards and Technology: Gaithersburg, MD, 2000; Vol. *2012*.

(30) Millero, F. J.; Graham, T. B.; Huang, F.; Bustos-Serrano, H. Pierrot, D. Dissociation Constants of Carbonic Acid in Seawater as a Function of Salinity and Temperature. *Mar. Chem.* **2006**, *100*, 80−94.

(31) Atkins, P.; De Paula, J. *Elements of Physical Chemistry*, 6th ed.; W.H. Freeman: New York, 2013.

(32) Brosillon, S.; Lhomme, L.; Vallet, C.; Bouzaza, A.; Wolbert, D. Gas Phase Photocatalysis and Liquid Phase Photocatalysis: Interdependence and Influence of Substrate Concentration and Photon Flow on Degradation Reaction Kinetics. *Appl. Catal., B* **2008**, *78*, 232−241.

(33) Emeline, A. V.; Ryabchuk, V.; Serpone, N. Factors Affecting the Efficiency of a Photocatalyzed Process in Aqueous Metal-oxide Dispersions - Prospect of Distinguishing Between Two Kinetic Models. *J. Photochem. Photobiol., A* **2000**, *133*, 89−97.

(34) Ciucci, F.; de Falco, C.; Guzman, M. I.; Lee, S.; Honda, T. Chemisorption on Semiconductors: The Role of Quantum Corrections on the Space Charge Regions in Multiple Dimensions. *Appl. Phys. Lett.* **2012**, *100*, 183106.

(35) Rossetti, R.; Hull, R.; Gibson, J. M.; Brus, L. E. Excited Electronic States and Optical Spectra of ZnS and CdS Crystallites in the ≅ 15 to 50 Å Size Range: Evolution from Molecular to Bulk Semiconducting Properties. *J. Chem. Phys.* **1985**, *82*, 552−559.

(36) Zhang, X. V.; Martin, S. T.; Friend, C. M.; Schoonen, M. A. A.; Holland, H. D. Mineral-Assisted Pathways in Prebiotic Synthesis: Photoelectrochemical Reduction of Carbon(+IV) by Manganese Sulfide. *J. Am. Chem. Soc.* **2004**, *126*, 11247−11253.

(37) Henglein, A.; Gutiérrez, M. Photochemistry of Colloidal Metal Sulfides. 5. Fluorescence and Chemical Reactions of ZnS and ZnS/CdS Co-Colloids. *Ber. Bunsen.-Ges. Phys. Chem.* **1983**, *87*, 852−858.

(38) Mills, A.; Le Hunte, S. An Overview of Semiconductor Photocatalysis. *J. Photochem. Photobiol., A* **1997**, *108*, 1−35.

(39) Cornu, C. J. G.; Colussi, A. J.; Hoffmann, M. R. Time Scales and pH Dependences of the Redox Processes Determining the Photocatalytic Efficiency of TiO_2 Nanoparticles from Periodic Illumination Experiments in the Stochastic Regime. *J. Phys. Chem. B* **2003**, *107*, 3156−3160.

(40) Bard, A. J.; Faulkner, L. R. *Electrochemical Methods: Fundamentals and Applications*; Wiley: New York, 2000.

(41) Zhao, J.; Holmes, M. A.; Osterloh, F. E. Quantum Confinement Controls Photocatalysis: A Free Energy Analysis for Photocatalytic Proton Reduction at CdSe Nanocrystals. *ACS Nano* **2013**, *7*, 4316−4325.

(42) Mohamed, H. H.; Bahnemann, D. W. The Role of Electron Transfer in Photocatalysis: Fact and Fictions. *Appl. Catal., B* **2012**, *128*, 91−104.